Journal of
Lightwave
Technology
A JOINT IEEE / OSA PUBLICATION

IEEE Xplore® Digital Library
http://ieeexplore.ieee.org/Xplore

# Microring-based Optical Isolator and Circulator with Integrated Electromagnet for Silicon Photonics

Paolo Pintus, *Member, IEEE*, Duanni Huang, Chong Zhang, Yuya Shoji, *Member, IEEE*, Tetsuya Mizumoto, *Fellow, IEEE*, and John E. Bowers, *Fellow, IEEE*,

***Abstract*— In this work, we present optical isolators and circulators fabricated by bonding cerium-substituted yttrium iron garnet (Ce:YIG) on silicon microring resonators. A novel integrated electromagnet is fabricated by depositing a metal micro-strip on the bonded chip. We experimentally prove that it can be efficiently used to control the magnetic field needed to induce the nonreciprocal phase shift effect in the Ce:YIG. The fabricated devices exhibit extremely small footprint (<70μm) and can be packaged, eliminating the need of a large size permanent magnet. A large optical isolation of 32 dB and 11 dB is measured for the isolator and the circulator, respectively. Moreover, a two-microring solution is also investigated to provide larger bandwidth and higher isolation. The proposed approach represents a promising solution for large scale integration of nonreciprocal components in silicon photonics.**

***Index Terms*— Magnetooptic devices, optical isolators, optical circulators, microresonators, integrated optoelectronics.**

## I. Introduction

NONRECIPROCAL components, such as optical isolators and circulators, are fundamental building blocks in optics to block undesirable back-reflections and to separate counter-propagating optical signals. Optical isolators are especially important as silicon photonic integrated circuits (PIC) grow in complexity [1], potentially introducing strong reflections especially at mode conversion tapers and transitions. On the other hand, integrated circulators would enable bidirectional operation in optical interconnects [2-4] and optical sensors [5].

To date, several approaches to achieve nonreciprocity on-chip have been proposed, although many challenges remain. Nonreciprocal devices are characterized by a symmetry breaking for the light that propagates from opposite directions, which results in an asymmetric scattering matrix. This is in contrast to optical diodes [6], which are completely comprised of purely reciprocal elements, and have the drawback of breaking down when forward and backwards propagating light are simultaneously passing through the structure [7]. For truly nonreciprocal devices, three different approaches have been proposed: i) nonlinear materials, ii) temporal-based modulation of the refractive index, and iii) magneto-optic (MO) materials [8,9]. However, only a few nonlinear optical phenomena such as Brillouin scattering can be effectively used to break the symmetry [10,11]. Some nonlinear effects such as the Kerr effect are currently under scrutiny over whether they truly provide isolation [12,13]. Pairs of electro-optic modulators operating in tandem can also be used to induce nonreciprocity, although multiple pairs are needed for effective isolation, which greatly increases the complexity of the device [14,15].

On the other hand, MO material can be effectively bonded on silicon-on-insulator (SOI) wafer, and both isolators and circulators can be realized with relatively simple design. The MO material becomes nonreciprocal when it is magnetized in a quasi-static magnetic field. Optical isolation using MO garnet can be performed using two configurations named Faraday and Voigt, respectively. In the former case, an external magnetic field is applied parallel to the wave propagation direction such that the polarization of light shows different rotation angle while it propagates forward or backward. In the latter one, the magnetic field is perpendicular to the propagating direction of light, which exhibits a different phase velocity according to the propagation direction [16,17]. Properly designed interferometric devices generate constructive interference for forward light and destructive interference for backward light achieving the isolating function. These devices are often designed in an unbalanced Mach-Zendner interferometer [18-21] or microring configuration [22-24]. However, the large absorption loss (e.g., 60 dB/cm) in MO material like cerium-substituted yttrium iron garnet (Ce:YIG) and the use of a permanent magnet for applying an external magnetic field are two important aspects that limit the performance and the

Manuscript received …; revised …; accepted … .

P. Pintus and D. Huang contributed equally to this work. This work was supported by the Air Force SBIR under Contract FA8650-15-M-1920 with Morton Photonics, the "Center for Scientific Computing at UCSB" and under NSF Grant CNS-0960316. The work of D. Huang was supported by National Science Foundation Graduate Research Fellowship Program.

P. Pintus is with the Department of Electrical and Computer Engineering, University of California, Santa Barbara, CA 93106 USA and also with TeCIP Institute, Scuola Superiore Sant'Anna Pisa 56124, Italy (e-mail: p.pintus@sssup.it, ppintus@ece.ucsb.edu).

D. Huang, C. Zhang, and J. E. Bowers are with the Department of Electrical and Computer Engineering, University of California, Santa Barbara, CA 93106 USA (e-mail: duanni@ece.ucsb.edu; czhang@ece.ucsb.edu; bowers@ece.ucsb.edu).

Y. Shoji and T. Mizumoto are with the Department of Electrical and Electronic Engineering/FIRST, Tokyo Institute of Technology, Tokyo 152-8552, Japan (e-mail: shoji.y.ad@m.titech.ac.jp; tmizumot@pe.titech.ac.jp).

Digital Object Identifier 10.1109/JLT.2016.2644626

integration of those devices moving forward. While the propagation loss can be greatly reduced in a device with small footprint, the external biasing magnet is still a significant limiting factor due to possible magnetic field interference with electronics and its large footprint (size>1mm$^2$).

In this work, exploiting Voigt configuration, we investigate integrated optical isolators and circulators using a planar spiral electromagnet that provides local control of the magnetic field, and can be easily integrated and packaged. This electromagnet should be placed in close proximity with the waveguide. We then experimentally verify our model by comparing it with fabricated isolators and circulators. A two-microring solution is also investigated to provide larger bandwidth and higher isolation.

## II. Device Design and Modelling

In a magneto-optic garnet, an external magnetic field is always needed to induce the nonreciprocal phase shift effect (NRPS). To avoid bulky magnets, an electric current can be efficiently used as a magnetic field source.

Using the direct wafer bonding approach [24-27], optical isolators and circulators can be manufactured for the transverse magnetic (TM) mode. Before bonding the magneto-optic garnet on the SOI wafer, the waveguides and microring resonators are patterned on the silicon layer. Because the field decreases with the distance between the waveguide and the electromagnet, the substrate of the bonded chip (SGGG in Fig. 1) is thinned to few micrometers. Next, a metallic micro-strip, aligned with the device underneath, is fabricated above the chip. A schematic of the device is shown in Fig. 1.

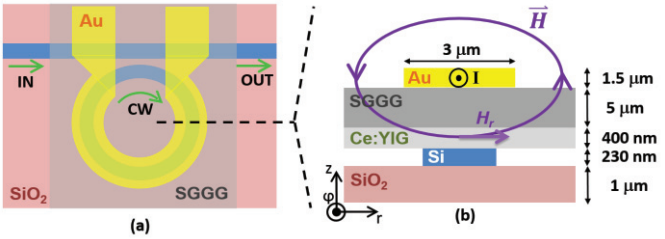


Fig. 1. (a) Top view of the isolator. (b) Cross-section of the microring resonator. The cylindrical coordinate system is shown in Fig. 1b as a reference frame. Pictures are not to scale.

In the following subsections, we present the modelling of the nonreciprocal magneto-optic split and the reciprocal thermal shift, the waveguide/microring cross-section optimization, and the electromagnet design.

### A. Magneto-optic split and thermal shift modelling

When a static radial magnetic field $H_r$ is applied, the clockwise (CW) and the counter clockwise (CCW) transverse magnetic modes in the microring have a different effective index and a split between their resonance wavelengths occurs [28]. The value of the resonance wavelength split (RWS) is

$$\Delta\lambda_M^0 = \frac{\Delta n_{eff}}{n_g}\lambda \tag{1}$$

where $\Delta n_{eff}$ is the effective index difference between CW and CCW mode, and $n_g$ is the average group index with respect to the two directions, both computed at room temperature (i.e., $T_{amb}$=20°C).

The RWS is proportional to the Faraday rotation constant, which is equal to -4500°/cm at room temperature for an in-plane (radial) magnetic field larger than 50 Oe [24]. Below the magnetic saturation, its value can be approximated as a hyperbolic tangent. Moreover, as the device heats up, the Faraday rotation will change by $d\theta_F/dT$=+44°/K [29]. Combining these two effects, we have

$$\theta_F(H_r,T) = \left[\theta_F^0 + \frac{d\theta_F}{dT}\left(T - T_{amb}\right)\right]\cdot\tanh\left(\frac{H_r}{H_r^0}\right) \tag{2}$$

where $\theta_F^0$=-4500°/cm and $H_r^0$=24 Oe [25]. As a result, below the saturation and for $T>T_{amb}$, the MO resonance wavelength split decreases and its value is rescaled as

$$\Delta\lambda_M(H_r,T) = \frac{\Delta\lambda_M^0}{\theta_F^0}\theta_F(H_r,T) \tag{3}$$

The DC current, used to generate the magnetic field, might also cause a local heating due to the Joule effect. From the electromagnetic modal analysis of the microring with respect to the temperature, the thermal (reciprocal) resonance wavelength shift is $\Delta\lambda_T$ valued as

$$\Delta\lambda_T = \frac{\lambda}{n_g}\left(\sum_i \frac{\partial n_{eff}}{\partial n_i}\frac{\partial n_i}{\partial T}\right)\Delta T \tag{4}$$

where the derivative $\partial n_i/\partial T$ depend on the materials with refractive index $n_i$, while $\partial n_{eff}/\partial n_i$ can be computed from the mode solver [30]. For the device under investigation, we computed a resonance wavelength shift of 71.6 pm/°C for the TM mode [25].

Including both thermal and MO contributions, the total resonance wavelength shift is

$$\Delta\lambda = \Delta\lambda_T(T) \pm \frac{1}{2}\Delta\lambda_M(H_r,T) \tag{5}$$

where ± refer to the CW and CCW modes, respectively.

### B. Waveguide Cross-section Optimization

A fully etched silicon waveguide is assumed in our design. The device is shown in Fig. 1. A silicon microring resonator is fabricated on a SOI wafer, having refractive index $n_{Si}$=3.48 and $n_{SiO2}$=1.46 at λ=1550nm, respectively. The microring is bonded with a Ce:YIG garnet ($n_{Ce:YIG}$=2.22) previously grown on a (Ca,Mg,Zr)-substituted gadolinium gallium garnet (SGGG), ($n_{SGGG}$=1.97). The remaining space is filled by air. At the interface between the Ce:YIG and the silicon, a thin silica ($SiO_2$) layer is considered, which is a byproduct of the oxygen plasma assisted bonding of the Ce:YIG. All materials

are low loss at λ=1550 nm, with the exception of the Ce:YIG which has a propagation loss of about 60 dB/cm, included in the mode analysis.

The nonreciprocal behavior of the hybrid Ce:YIG/Si waveguide is analyzed using an accurate nonreciprocal mode solver based on the finite element method [30]. The silicon waveguide cross-section is designed to maximize the RWS in Eq. (1) [25, 28]. In [28] the waveguide cross-section has been optimized assuming $\theta_F$=-4000°/cm and no $SiO_2$ bonding layer, while in [25] $\theta_F$=-4500°/cm and a 10 nm thick oxide layer are considered. Nevertheless, the optimum cross-sections in the two cases are very similar.

Assuming a 230nm × 600nm silicon waveguide cross-section, and 400 nm thick Ce:YIG layer, we investigate the degradation of the RWS with respect to the bonding oxide layer thickness. As shown in Fig. 2(a), the oxide layer thickness must be precisely controlled in order to provide a large RWS. On the other hand, large variation on the silicon waveguide width ($\Delta w_{Si}$), the silicon waveguide thickness ($\Delta h_{Si}$), and the Ce:YIG thickness ($\Delta h_{Ce:YIG}$) are less critical, as shown in Fig. 2(b) for a comparison with silica thickness ($\Delta h_{SiO2}$).

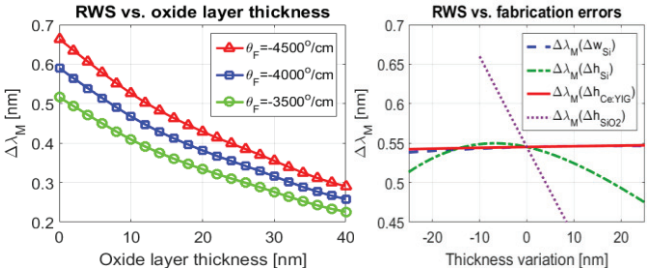


Fig. 2. (a) RWS computed with respect to the Faraday rotation constant and the silica bonding layer thickness. (b) RWS variation with respect to the fabrication error for $\theta_F$=-4500°/cm assuming $h_{Si}$=230nm, $w_{Si}$=600nm, $h_{Ce:YIG}$=230nm, and $h_{SiO2}$=10nm.

### C. *Single and Multi-Coil Electromagnet*

The electromagnet can be fabricated on the back-side of the SGGG substrate, which has been thinned to reduce the distance between the current and the Ce:YIG layer. In order to provide a large magnetic field while limiting the heating, a large current and a small resistance are required. For this purpose, a single gold microstrip coil is designed with a 3 µm wide and 1.5 µm thick cross-section [25].

The radial magnetic field and the temperature distribution have been computed using COMSOL Multiphysics software. In Fig. 3(a), the intensity of $H_r$ at the Si/Ce:YIG interface is shown as a function of the electromagnet current ($I$) and the SGGG thickness. For the same input values, the average temperature increment ($\Delta T=T-T_{amb}$) in the silicon microring is reported in Fig. 5b.

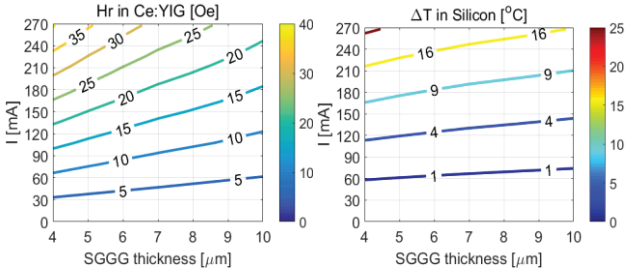


Fig. 3. (a) Radial magnetic field at the silicon/Ce:YIG interface (b) average temperature variation in the silicon microring for a microring radius of 35µm. In both plots the current and the SGGG thickness are varied.

From the numerical results in Fig. 3, for a fixed current value, the magnetic field is much more sensitive to the SGGG thickness than the temperature. Moreover, for a fixed SGGG thickness, the magnetic field scale linearly with the current while $\Delta T$ varies quadratically with the current, as expected. The same behaviour is better visible in Fig 5.

To increase the radial magnetic field without further thinning the SGGG layer, which can be challenging to fabricate, a multi-loop spiral solution is preferred [31]. For multiple-loop, two level of metal are needed. In Fig. 4, the numerical results are reported for the 3 loop spiral integrated planar electromagnet. The intensity of $H_r$ at the Si/Ce:YIG interface is shown in Fig. 4(a) assuming $I$=180 mA and 5 µm-thick SGGG substrate. Under the same condition the temperature distribution $\Delta T$ is shown in Fig. 4(b). From both images, it is clear that the magnetic field and temperature variation are local and do not affect devices that are relatively far from it.

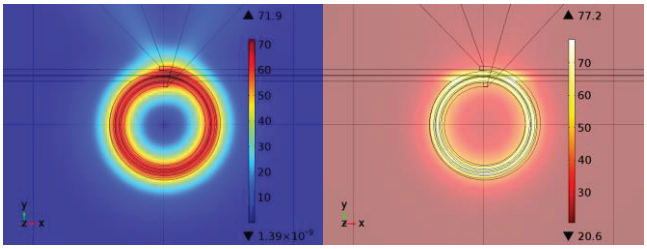

Fig. 4. Multiphysics simulation resuts: a) radial magnetic field generated by the electric current I=180 mA, b) temperature distribution in the device

The performance of single loop, 3-loops and 5-loops are compared. In Fig. 5(a), the magnetic field in the Ce:YIG is computed as a function of the injected current for 5 µm-thick SGGG layer. For the same value, the temperature in the silicon is reported in Fig. 5(b). Those simulations results can be effectively used to compute $\Delta\lambda_M$ and $\Delta\lambda_T$ described by Eq. (3) and Eq. (4), respectively. Those simulations are key to understanding the behavior of the device at different driving currents.

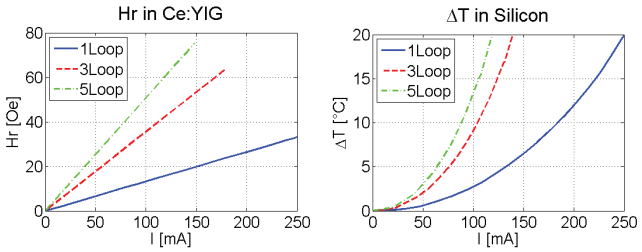


Fig. 5. Electromagnet comparison (a) radial magnetic field at the silicon-Ce:YIG interface (b) average temperature variation in the silicon microring

### D. *Model Validation*

We experimentally validate the model by testing a nonreciprocal microring-based device with a single coil electromagnet. For a fixed DC current, we record the transmittance of the device as we sweep the tunable laser wavelength, and repeat the measurements for the backwards transmission. The split between the two resonances is measured directly from the forward and backward spectra, while $\Delta\lambda_T$ is computed as the average shift of the CW and CCW wavelength resonances with respect to the resonance at I=0. In Fig. 6, we see a clear resonance split of roughly 0.32nm for 140mA of applied current (roughly 20 Oe of applied field) and a thermally induced redshift of 0.4 nm.

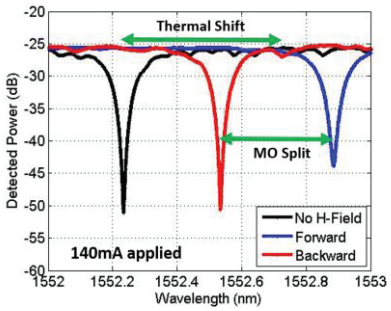


Fig. 6. Experimental results showing both the MO nonreciprocal wavelength split as well as the reciprocal thermally induced redshift.

Reversing the direction of the current, produces a field with same amplitude but opposite direction while the heating is unchanged. As a result, we can write

$$\Delta\lambda(I) = \Delta\lambda_T(I) - \frac{1}{2}\Delta\lambda_M(I) \tag{6a}$$

$$\Delta\lambda(-I) = \Delta\lambda_T(-I) + \frac{1}{2}\Delta\lambda_M(-I) \tag{6b}$$

where $I$ is the electromagnet current. From the previous relations, $\Delta\lambda_M$ are $\Delta\lambda_T$ can be easily derived. A comparison between the model and the experimental results is shown in Fig. 7 as a function of the coil-current for different layer thickness and microring radius. For 5 µm-thick SGGG substrate and 35 µm microring radius, the RWS and the thermal shift are shown in Fig. 7(a) and Fig. 7(c), respectively. Analogous results are shown in Fig. 7(b) and Fig. 7(d) for a SGGG layer of 8 µm and R=20 µm. All the derived results show an excellent agreement between the experiments and simulations.

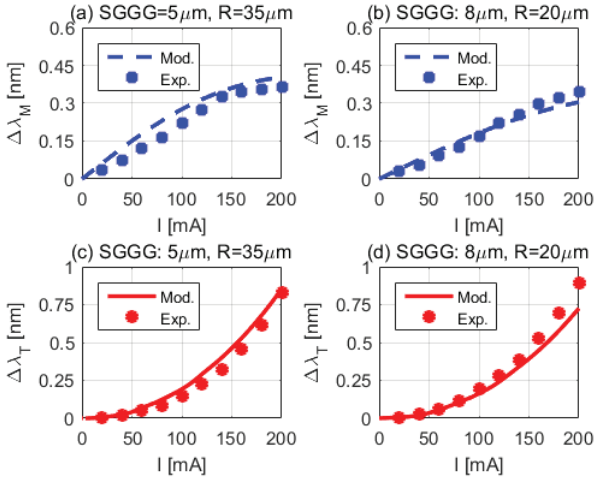


Fig. 7. Experiment and simulation comparison of a single coil electromagnet (a) $\Delta\lambda_M$ for 5 µm-thick SGGG and 35 µm microring radius, (b) $\Delta\lambda_M$ for 8 µm-thick SGGG and 20 µm microring radius, (c) $\Delta\lambda_T$ for 5 µm-thick SGGG and 35 µm microring radius, (d) $\Delta\lambda_T$ for 8 µm-thick SGGG and 20 µm microring radius.

The thermal dissipation and consequent resonant wavelength shift $\Delta\lambda_T$ can be reduced by decreasing the spiral resistance, e.g. depositing a thicker metal trace or widening the microstrip footprint.

## III. Integrated Optical Isolator

An optical isolator can be fabricated using a straight waveguide coupled to a single microring resonator (all-pass microring filter) as shown in Fig. 1(a). In this case, the forward propagating light is coupled to the CW mode, while the backward light is coupled to the CCW mode. When the optical input is set off-resonance for the CW and on-resonance for the CCW, the forward light is transmitted while the backward light is filtered and radiated out by the microring. To maximize the isolation, the coupling between the waveguide and the microring must have its critical value [28].

### A. *All-Pass Single Microring Isolator*

Recently, we have experimentally demonstrated a large isolation in a nonreciprocal all-pass single microring isolator with a 35 µm microring radius. A 32 dB of isolation is measured near 1555 nm with only 2.3 dB of excess loss to silicon [25].

Fig. 8 shows the measured optical isolation as a function of the injected current. The NRS is also reported at the bottom axis of the same figure. An optical isolation larger than 25 dB is measured for I between 40 mA and 180 mA. For small value of current (I < 40 mA), the resonances of the CW and CCW mode are too close. On the other hand, for larger values of current, the microring heats up and it moves out of the critical coupling condition, causing the isolation to drop. For I = 180 mA, a thermal shift up to 0.75 nm is reached (see Fig. 7(c)). This result suggests that the thermal effect can be used to finely tune the microring resonator in order to

compensate unavoidable fabrication errors. However, further design optimization is needed.

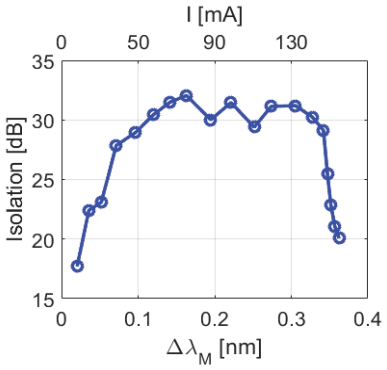


Fig. 8. Optical isolation as a function of the current (top-axes) and the nonreciprocal resonance wavelength split (bottom-axes).

Resonant-based filters are highly selective in wavelength so a microring-based isolator can effectively isolate the narrow-linewidth output signal of a laser. For some applications (e.g., modulated signal or sensors), the bandwidth of a single microring can be too narrow and multi-microring isolators can successfully be used to enlarge the bandwidth and the isolation [32].

### *B. Cascaded Ring Isolator*

The optical isolation bandwidth can be effectively enlarged by cascading two identical optical isolators, as shown in Fig. 9. To provide the largest isolation, the amplitudes of the currents in the two electromagnet are chosen such that the CCW resonances of the two microrings are aligned with the input signal wavelength ($\lambda_{IN}$), while the CW resonances fall apart, at higher and lower wavelength, respectively. A schematic plot of each isolator spectra and the cascaded transfer function are shown in Fig. 9. The light propagates from IN-port to OUT-port without obstacle, while in the opposite direction the light is coupled into the rings.

In the two electromagnets, the currents flow in opposite directions to provide the opposite nonreciprocal wavelength split direction shown in Fig. 9.

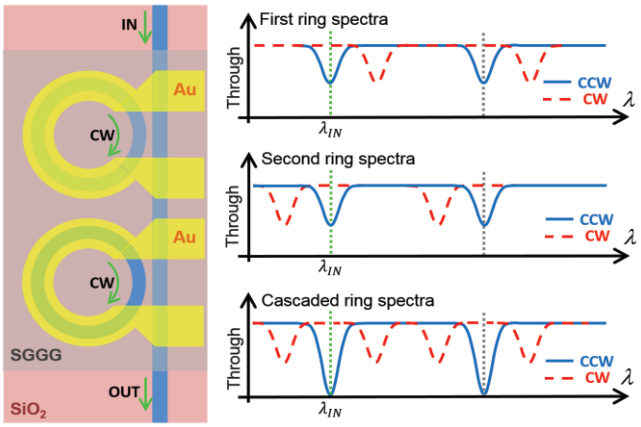


Fig. 9. (left) Cascaded microring-based isolator. (right) Transfer functions of the first isolator, second isolator and final transfer function. Pictures are not to scale.

The fabricated devices are shown in Fig. 10, where the SGGG layer is 5 μm thick, the radius of both microrings is 20 μm, and the distance between their centers is set to 100 μm. The microring-waveguide coupling distance is varied from 200 nm up to 260 nm, therefore different coupling coefficients are realized.

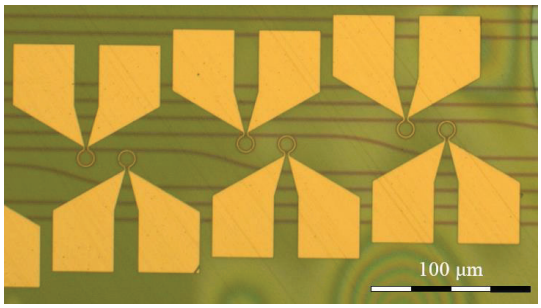


Fig. 10. Microscope image of the fabricated device with splits for various microring-waveguide coupling distances.

For a microring-waveguide coupling distance of 230 nm, the experimental total resonance wavelength shift of both microrings is shown in Fig. 11. In this device, the critical coupling condition is achieved for λ~1460 nm. In Fig. 11(a) the current in the first isolator ($I_1$) is swept from -240 mA to 240 mA, while the current in the second isolator ($I_2$) is zero. Vice versa, in Fig. 11(b) $I_1$=0 and $I_2$ is swept from -240 mA to 240 mA.

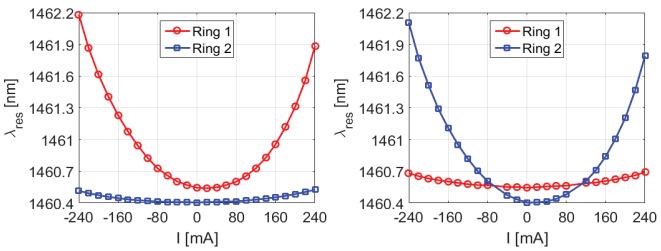


Fig. 11. Experimental total resonance wavelength shift of the two microrings: (a) the current in the first isolator is swept while $I_2$=0, (b) the current in the second isolator is swept while $I_1$=0.

Although the microrings are designed to be identical, when $I_1$=$I_2$=0, the two resonances are not aligned due to small fabrication errors, and their values are $\lambda_{res,1}$=1460.54 nm and $\lambda_{res,2}$=1460.40 nm for microring 1 and microring 2, respectively. A slightly different current amplitude is injected so that the different thermal heating can be used to align the CCW-spectra and compensate the fabrication variation.

Considering the relations in Eq. (6), the nonreciprocal wavelength split and the thermal shift are derived for both microrings when $I_1$≠0 and $I_2$=0, as shown in Fig. 12(a). The nonreciprocal phase shift of microring 1 reaches the maximum value of 0.302 nm for $I_1$=200mA while the thermal shift is about 0.919 nm. Under this condition, the resonance of the second microring can slightly vary due to the thermal cross-talk (i.e., 0.075 nm) while the magnetic field cross-talk is negligible. Because the geometry of the devices is symmetric, very similar results can be obtained when $I_1$=0 and $I_2$≠0, as shown in Fig. 12(b).

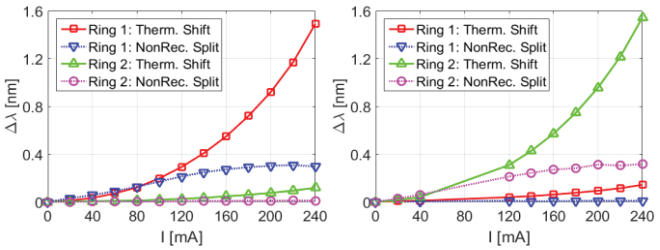


Fig. 12. (a) Nonreciprocal wavelength split and the thermal shift in the two microrings when the amplitude of $I_1$ varies form 0 to 240 mA and $I_2$=0, (b) Nonreciprocal wavelength split and the thermal shift in the two microrings when the amplitude of $I_1$=0 and $I_2$ varies form 0 to 240 mA.

For λ~1500 nm, the critical coupling condition is reached for a microring-waveguide coupling distance of about 200 nm. In this case, the optimal current values in the two electromagnet are $I_1$ = 195 mA and $I_2$ = -170 mA for the first and the second isolator, respectively. The experimental results are shown in Fig. 13(a), the CCW resonance of the two microrings are aligned and an isolation of about 28 dB is measured at $\lambda_{IN}$=1503.7 nm. The measured isolation is slightly lower than the single microring isolator because both microrings must work at the critical coupling condition. However, the slight different temperature might affect this condition.

The isolation of a signal with a non-negligible bandwidth is computed as

$$IR = \int |S_{CW}(\lambda)|^2 / |S_{CCW}(\lambda)|^2 \, d\lambda \qquad (7)$$

where $S_{CW}(\lambda)$ and $S_{CCW}(\lambda)$ are transition spectra of the whole device in the forward and backward direction, respectively. If $\lambda_{IN}$ is the input wavelength and BW is the considered bandwidth, the integral is computed from $\lambda_{IN}$ - BW/2 and $\lambda_{IN}$ + BW/2. The optical isolations of fabricated single and two-cascaded microring isolator are plotted as a function of the signal bandwidth in Fig. 13(b), showing a larger isolation bandwidth for the cascaded-microring isolator.

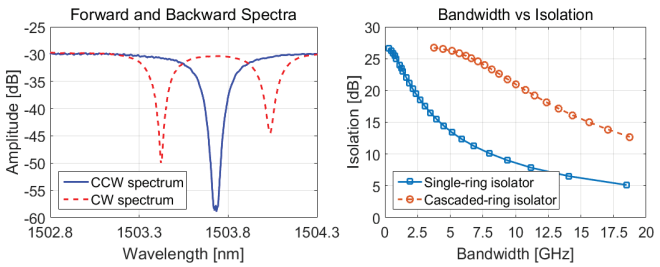


Fig. 13. (a) Experimental forward and backward spectra of two-cascaded microring isolator. (b) comparision of optical isolation in fabricated single and two-cascaded microring isolators with respect to the isolation bandwidth.

## IV. Integrated Optical Circulator

A microring-based optical circulator can be performed using a microring add/drop filter, as proposed in [33,34]. In the following sections we present the experimental results for a single microring device and then the improvement can be achieved in term of bandwidth and isolation in a two-microring circulator.

### A. Four-port Add-Drop Microring Circulator

The optimization of a four-port microring circulator is detailed in [33]. Using the same design rules, an integrated optical circulator is fabricated and characterized for TM mode with bonded Ce:YIG. The device is schematically shown in Fig. 14 (a). The fabricated devices are shown in Fig. 14(b), where the SGGG layer is 8 μm thick and the microring radius is 20 μm.

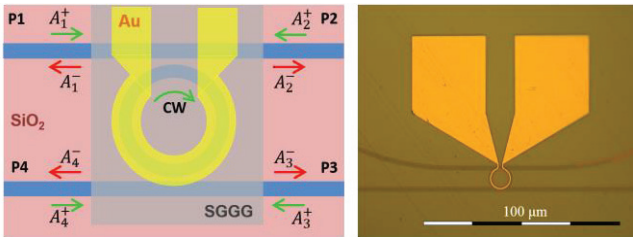


Fig. 14. (a) Schematic structure of the TM-mode four-port optical circulator, pictures is not to scale, (b) microscope image of the fabricated device.

The closed four-port characteristics of the device can be easily verified. Indeed, when the CW and CCW resonances are differentiated and the input signal matches the CCW resonance of the nonreciprocal microring, the circulating direction is P1→P2→P3→P4→P1. Vice versa, when the signal wavelength matches the CW resonance wavelength, the circulating direction is reversed.

If the waveguide backscattering is negligible and the gaps between the microring and the two waveguides are the same [33], the input/output relation can be effectively described by the following simplified scattering matrix

$$\begin{pmatrix} A_1^- \\ A_2^- \\ A_3^- \\ A_4^- \end{pmatrix} = \begin{pmatrix} 0 & S_{12} & 0 & S_{14} \\ S_{21} & 0 & S_{41} & 0 \\ 0 & S_{14} & 0 & S_{12} \\ S_{41} & 0 & S_{21} & 0 \end{pmatrix} \begin{pmatrix} A_1^+ \\ A_2^+ \\ A_3^+ \\ A_4^+ \end{pmatrix} \qquad (8)$$

where $A_i^+$ (for i=1,2,3,4) is the field that travel toward the circulator from port Pi. and $A_i^-$ (for j=1,2,3,4) is the field that leave the microring from port Pj. To perform the P1→P2→P3→P4→ P1, $|S_{12}|$ and $|S_{41}|$ must be smaller compared to $|S_{21}|$ and $|S_{14}|$ [33].

The simulated and the experimental spectra are shown in Fig. 15. The plots show a very good agreement between theory and measurements. However, the unavoidable fabrication inaccuracy might cause small geometry variation and so a shift of the spectra with respect to the simulated ones. To better compare the spectra, the simulated ones have been blueshifted by 0.633nm to be aligned with the experiments. The dashed line in the figure indicates the CCW resonance wavelength.

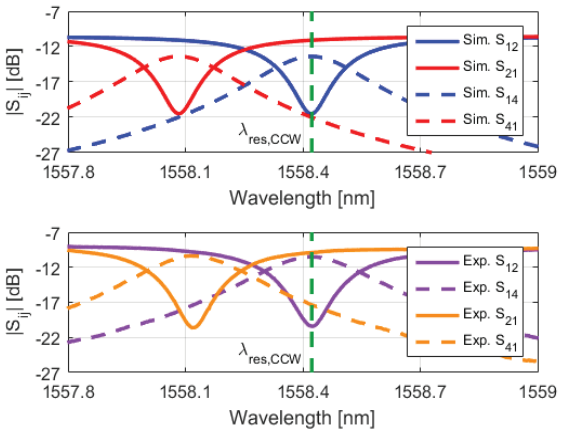


Fig. 15. Simulated (top) and measured (bottom) scattering coefficients of the single microring four-port optical circulator.

Because the bonded chip is 3.5mm long, the propagation loss in the input/output waveguide is estimated to be 8.7 dB due to the large absorption of the Ce:YIG. Nevertheless, it can be strongly reduced by removing the areas of the bonded chip that are not covering the microring. The measured optical isolation at $\lambda_{res,ccw}$=1558.38 between adjacent ports is 11 dB between port P1 and port P2 (i.e.,$IR_{12} = |S_{21}|/|S_{12}|$), and 6.7 dB between port P1 and P4 (i.e., $IR_{41} = |S_{14}|/|S_{41}|$) [35]. The two isolation ratios $IR_{12}$ and $IR_{41}$ differ because the estimated coupling coefficient in the fabricated device (K=10.45%) is larger than the optimum value for $\Delta\lambda_M = 0.35$, which is K=9.0%. In Fig. 15, the simulated coefficients are computed in the former case.

### *B. Coupled Microring Circulator*

A second order filter can be effectively used to enlarge the optical isolation and the isolation bandwidth. The schematic view of the two-microring circulator is shown in Fig. 16 and its scattering matrix is like the one of Eq. (8).

The light in the two microrings in Fig. 16 propagates in opposite directions. As a result, to properly align the miroring resonances, the current in the two electromagnet must have the same intensity but opposite direction.

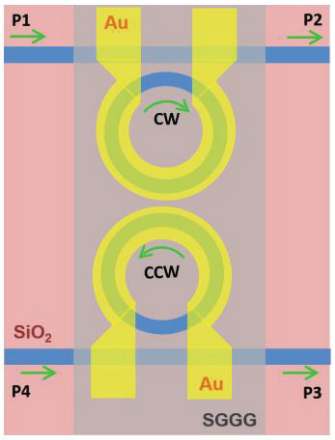


Fig. 16. Schematic structure of the two-microring four-port optical circulator. Pictures is not to scale.

The performance of the simulated two-microring isolator is compared with the simulated single-microring circulator. For the single microring, we assumed a waveguide-microring power coupling coefficient of 9%, while in the two-microring device the waveguide-microring and microring-to-microring power coupling coefficients are 13.16% and 0.5%, respectively [36]. For both devices the microring radius is 20 μm and the SGGG is 8 μm thick. The magnitude of the simulated scattering coefficients is shown in Fig. 17.

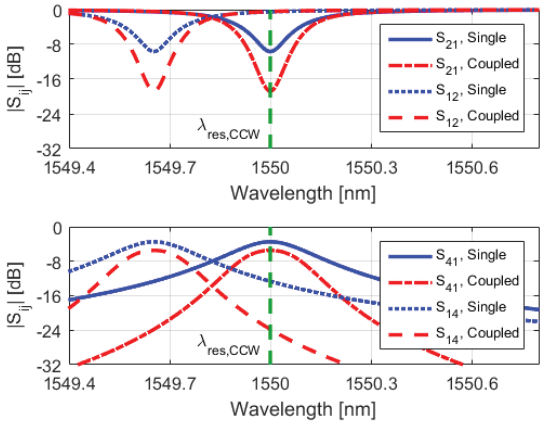


Fig. 17. Simulated spectra of single and two- microring circulators.

For the single microring circulator, the isolation ratio is $IR_{12} = IR_{41} = 9.15$ dB at $\lambda_{res,ccw}$=1550 nm, while double for the coupled microring device, $IR_{12} = IR_{41} = 18.3$ dB. Similarly, the isolation bandwidth is double for a fixed isolation ratio, as shown in Fig. 18.

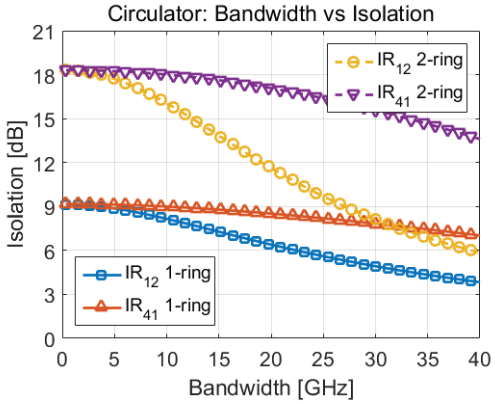


Fig. 18. Comparision of simulated optical isolation in single and two-microring circulators with respect to the isolation bandwidth.

Note that the isolation of the simulated single-microring circulator is lower (i.e., 9dB) than largest isolation in the fabricated one (i.e., 11dB). However, in the former case all ports have the same isolation ratio, while in the latter case their values are quite unbalanced (i.e., 11dB and 6.7dB).

## V. Conclusion

In this work, we present a comprehensive examination of the performance of single-microring and two-microring integrated optical isolators and circulators. The experimental

results have been compared with a reliable mathematical model, showing excellent agreement. Some promising improvements, like the multi-coil electromagnet and the coupled-microring circulator, have been proposed and investigated. Although those devices work only for the TM polarized light, transverse electric isolator and circulator can be fabricated by adding polarization rotators at the input. The proposed approach represents a viable solution in integrated optics, proved by the large isolation and small footprint. Moreover, the proposed electromagnet can provide local control of the magnetic field, eliminating the need for a bulky permanent magnet and easing packaging requirements. Finally, the current induced magnetic field can be switched and modulated, leading to a new class of magneto-optic devices for silicon photonics.

## VI. Acknowledgment

The authors thank Paul Morton, Jacob Khurgin, Jon Peters, Daryl Spencer, Michael Davenport, Lin Chang, Tin Komljenovic and Fabrizio Di Pasquale for helpful discussions.

## VII. References

[1] C. Zhang, S. Zhang, J. D. Peters, and J. E. Bowers, "8×8×40 Gbps fully integrated silicon photonic network on chip," *Optica*, vol. 3, no. 7, pp. 785-786, 2016.

[2] K. Tai, B. Chang, J. Chen, C.H. Mao, T. Ducellier, J. Xie, L. Mao, and J. Wheeldon, "Wavelength-interleaving bidirectional circulators," *IEEE Photon. Technol. Lett.*, vol. 13, no. 4, pp 320-322, 2001.

[3] P. Pintus, N. Andriolli, F. Di Pasquale, and J. E. Bowers, "Bidirectional Crosstalk and Back-Reflection Free WDM Active Optical Interconnects," *IEEE Photon. Technol. Lett.*, vol. 25, no. 20, pp. 1973-1976, 2013.

[4] D. Dai and J. E. Bowers, "Silicon-based on-chip multiplexing technologies and devices for Peta-bit optical interconnects," *Nanophotonics*, vol. 3, no. 4-5, pp. 283-311, 2014.

[5] B. Lee and Y. Jeong, "Interrogation techniques for fiber grating sensors and the theory of fiber gratings," Fiber Optic Sensors; Edited by S. Yin, P.B. Ruffin, F.T.S. Yu, pp. 253-331, CRC Press, 2008.

[6] L. Fan, J. Wang, L. T. Varghese, H. Shen, B. Niu, Y. Xuan, A. M. Weiner, and M. Qi, "An all-silicon passive optical diode," *Science*, vol. 335, no. 6067, pp. 447-450, 2012.

[7] D. Jalas, A. Petrov, M. Eich, W. Freude, S. Fan, Z. Yu, R. Baets, M. Popovic, A. Melloni, J. Joannopoulos, M. Vanwolleghem, C. Doerr, and H. Renner, "What is - and what is not - an optical isolator", *Nat. Photonics*, vol. 7, no. 8, pp. 579-582, 2013.

[8] B. J. Stadler and T. Mizumoto, "Integrated magneto-optical materials and isolators: a review," *IEEE Photon. J.*, vol. 6, no. 1, pp. 1-15, 2014.

[9] Y. Shoji and T. Mizumoto, "Magneto-optical non-reciprocal devices in silicon photonics", *Sci. Technol. Adv. Mat.*, vol. 15, no. 1, p. 014602, 2014.

[10] C. G. Poulton, R. Pant, A. Byrnes, S. Fan, M. J. Steel, and B. J. Eggleton, "Design for broadband on-chip isolator using stimulated Brillouin scattering in dispersion-engineered chalcogenide waveguides," Opt. Express. 20, 21235-46, (2012).

[11] C. H. Dong, Z. Shen, C. L. Zou, Y. L. Zhang, W. Fu, and G. C. Guo, "Brillouin-scattering-induced transparency and non-reciprocal light storage," *Nat. Commun.*, vol. 6, 2015.

[12] S. Hua, J. Wen, X. Jiang, Q. Hua, L. Jiang, and M. Xiao, "Demonstration of a Chip-based Nonlinear Optical Isolator," arXiv preprint arXiv:1606.04400, 2016.

[13] Y. Shi, Z. Yu, and S. Fan, "Limitations of nonlinear optical isolators due to dynamic reciprocity," *Nat. Photon*., vol. 9, no. 6, pp. 388-392, 2015.

[14] C. R. Doerr, N. Dupuis, and L. Zhang, "Optical isolator using two tandem phase modulators," *Opt. Lett.*, vol. 36, no. 21, pp. 4293-4295, 2011.

[15] C. R. Doerr, L. Chen, and D. Vermeulen, "Silicon photonics broadband modulation-based isolator," *Opt. Express*, vol. 22, no. 4, pp. 4493-4498, 2014.

[16] Y. Shoji, K. Miura, and T. Mizumoto, "Optical nonreciprocal devices based on magneto-optical phase shift in silicon photonics," *J. Opt.*, vol. 18, no. 1, p. 013001, 2015.

[17] R. L. Espinola, T. Izuhara, M. C. Tsai, R. M. Osgood, and H. Dötsch, "Magneto-optical nonreciprocal phase shift in garnet/silicon-on-insulator waveguides," *Opt. Lett.*, vol. 29, no. 9, pp. 941-943, 2004.

[18] Y. Shoji, T. Mizumoto, H. Yokoi, I. W. Hseih, and R. M. Osgood Jr, "Magneto-optical isolator with silicon waveguides fabricated by direct bonding," *Appl. Phys. Lett.*, vol. 92, no. 7, p. 071117, 2008.

[19] Y. Shoji, M. Ito, Y. Shirato, and T. Mizumoto, "MZI optical isolator with Si-wire waveguides by surface-activated direct bonding", *Opt. Express*, vol. 20, no. 16, pp. 18440-18448, 2012.

[20] K. Mitsuya, Y. Shoji, and T. Mizumoto, "Demonstration of a silicon waveguide optical circulator," *IEEE Photon. Technol. Lett.*, vol. 8, no. 25, pp. 721-723, 2013.

[21] S. Ghosh, S. Keyvaninia, W. Van Roy, T. Mizumoto, G. Roelkens, and R. Baets, "Adhesively bonded Ce: YIG/SOI integrated optical circulator," *Opt. Lett.*, vol. 38, no. 6, pp. 965-967, 2013.

[22] N. Kono, K. Kakihara, K. Saitoh, and M. Koshiba, "Nonreciprocal microresonators for the miniaturization of optical waveguide isolators," *Opt. Express*, vol. 15, no. 12, pp. 7737–7751, 2007.

[23] D. Jalas, A. Petrov, M. Krause, J. Hampe, and M. Eich, "Resonance splitting in gyrotropic ring resonators," *Opt. Lett.*, vol. 35, no. 20, pp. 3438–3440, 2010.

[24] M. C. Tien, T. Mizumoto, P. Pintus, H. Kroemer, and J. E. Bowers, "Silicon ring isolators with bonded nonreciprocal magneto-optic garnets," Opt. Express, vol. 19, no. 12, pp. 11740-11745, 2011.

[25] D. Huang, P. Pintus, C. Zhong, Y. Shoji, T. Mizumoto, and J. E. Bowers, "Electrically driven and thermally tunable integrated optical isolators for silicon photonics," *IEEE J. Sel. Topics Quantum Electron*., vol. 22, no. 6, pp. 1-8, 2016.

[26] T. Komljenovic, M. Davenport, J. Hulme, A. Y. Liu, C. T. Santis, A. Spott, S. Srinivasan, E. J. Stanton, C. Zhang, and J. E. Bowers, "Heterogeneous Silicon Photonic Integrated Circuits," *J. Lightwave Technol.*, vol. 34, no. 1, pp. 20-35, 2016.

[27] M. J. R. Heck, J. F. Bauters, M. Davenport, J. K. Doylend, S. Jain, G. Kurczveil, S. Srinivasan, Y. Tang, and J. E. Bowers, "ybrid silicon photonic integrated circuit technology," *IEEE J. Sel. Topics Quantum Electron.*, vol. 19, no. 4, p. 6100117, 2013.

[28] P. Pintus, M.-C. Tien, and J. E. Bowers, "Design of magneto-optical ring isolator on SOI based on the finite element method," *IEEE Photon. Technol. Lett.*, vol. 23, no. 22, pp. 1670-1672, 2011.

[29] K. Furuya, T. Nemoto, K. Kato, Y. Shoji, T. Mizumoto, "Athermal operation of a waveguide optical isolator based on canceling phase deviations in a Mach-Zehnder interferometer," *J. Lightwave Technol.*, vol. 34, no. 8, p. 1699-1705, 2016.

[30] P. Pintus, "Accurate vectorial finite element mode solver for magneto-optic and anisotropic waveguides", *Opt. Express*, vol. 22, no. 13, pp. 15737-15756, 2014.

[31] P. Pintus, D. Huang, C. Zhang, Y. Shoji, T. Mizumoto, J. E. Bowers, "Novel Nonreciprocal Devices with Integrated Electromagnet for Silicon Photonics," W.3.F.3 in Proc. of 42nd European Conference on Optical Communication (ECOC 2016), Düsseldorf, Germany, Sep. 18-22, 2016.

[32] P. Pintus, F. Di Pasquale, and J. E. Bowers. "Design of transverse electric ring isolators for ultra-low-loss $Si_3N_4$ waveguides based on the finite element method," *Opt. Lett.*, vol. 36, no. 23, pp. 4599-4601, 2011.

[33] P. Pintus, F. Di Pasquale, and J. E. Bowers, "Integrated TE and TM optical circulators on ultra-low-loss silicon nitride platform," *Opt. Express*, vol. 21, no. 4, pp. 5041-5052, 2013.

[34] D. Jalas, A. Yu. Petrov, and M. Eich, "Optical three-port circulators made with ring resonators," *Opt. Lett.*, vol. 39, no. 6, pp. 1425-1428, 2014.

[35] D. Huang, P. Pintus, C. Zhong, P. Morton, Y. Shoji, T. Mizumoto, and J. E. Bowers, "Dynamically reconfigurable integrated optical circulators," *Optica*, vol. 4, no. 1, pp. 23-30, 2017.

[36] C. L. Manganelli, P. Pintus, F. Gambini, D. Fowler, M. Pourier, C. Kopp, F. Di Pasquale, and C. J. Oton, "Design of coupled micro-ring resonators for silicon photonic switching matrices," pp. 84-85, in Proc. of IEEE Optical Interconnects Conference (OI 2016), San Diego, CA, 2016.